


# Non-linear finite element modelling of light-to-heat energy conversion applied to solar nanofluids

Josep Forner-Escrig <sup>a</sup>, Rosa Mondragón<sup>a,\*</sup>, Leonor Hernández<sup>a</sup>, Roberto Palma<sup>b</sup>

<sup>a</sup>*Department of Mechanical Engineering and Construction, Universitat Jaume I, Av. de Vicent Sos Baynat, s/n 12071 Castellón de la Plana, Spain*

<sup>b</sup>*Department of Structural Mechanics and Hydraulic Engineering, University of Granada, Spain*

---

## Abstract

Nanoparticles (NPs) exhibit remarkable photothermal conversion efficiency under optical illumination. This light-induced heating on NPs is interesting in many different applications, such as solar radiation absorption in nanofluids, which the present work focuses on. Consequently, mastering the temperature increase undergone by NPs and the surrounding media is extremely relevant today. As nanothermometry measurements of a single NP are hard to obtain, numerical simulations can contribute to better understand the physical phenomena involved in light-induced heating. In this vein, the current work presents theoretical and numerical formulations to predict the heating of optically excited NPs. Theoretically, a thermodynamic approach is conducted to obtain balance and constitutive equations. These equations are numerically discretised in the finite element method and implemented into a research code. The main novelty of the present work lies in developing, from a multiphysics perspective, a time domain formulation capable of modelling instantaneous dissipation that can be easily extended to account for more physical phenomena. Finally, the numerical model is validated by comparing analytical and numerical results, and maximum values of 0.0014 (%) of relative error between them are reached. Then some different analysis are performed for gold, silver and graphite NPs of 20 (nm) in diameter to characterise the temperature increase they produce in the surrounding medium (water) when optically excited at a wavelength of 400 (nm) and a laser intensity of  $5 \times 10^4$  (W/cm<sup>2</sup>) –silver NPs exhibiting the most significant temperature increase. The influence of NP concentration on the increase of temperature in nanofluids

is numerically assessed as well by testing values of NP concentration up to a maximum of 0.052 (%), which considerably enhances temperature increase. In conclusion, the present numerical tool could be used to predict light-induced heating in NPs, which could complement and reduce the number of experiments for optimising the photothermal efficiency of solar nanofluids.

*Keywords:* Finite Element Method, Energy conversion, Light-to-heat, Multiphysics, Nanoparticles

---

## 1. Introduction

Nowadays, society's development is directly related to consumption of energy: generating and supplying energy are vital for human current lifestyle. However, producing that energy sustainably is of key importance to stop climate change and to preserve our natural environment for future generations. For this reason, use of renewable energies is increasing to take advantage of natural resources (inexhaustible on the human timescale) to produce clean energy. Of the wide variety of renewable energies, solar energy is particularly interesting for its enormous potential; for instance, it is estimated that around 30 minutes of solar irradiation on Earth equals one-year of the world's energy demand [1]. Although there are several solar energy technologies [2], the current work focuses on solar thermal energy.

Solar thermal energy is the name given to the thermal energy obtained from solar radiation. Its working principle consists of capturing the energy of light on an absorbing surface to transfer that energy to a heat carrier fluid [3]. One of the most widely used technologies to harness solar energy by converting light into thermal energy is solar collectors, for which two main collector configurations exist [4]:

- Tube-in-plate collectors, composed of selective absorbing surfaces that transfer solar-radiated heat to the working fluid. However, this technology has one main

---

\*Corresponding author

*Email address:* [mondrag@uji.es](mailto:mondrag@uji.es) (Rosa Mondragón)

*Preprint submitted to International Journal of Mechanical Sciences*

*25th June 2020*

drawback: the maximum temperature is reached on the collector's surface, which increases thermal losses [3]. Then the configuration of this collector cannot be optimal because the biggest differences in temperature appear between the surface collector and the carrier fluid flowing inside the tubes beneath. Therefore, tube-in-plate collectors present low thermal conversion efficiency.

- Volumetric collectors [5], which absorb solar energy directly within the fluid itself. For this purpose, thermal trapping tubes [6] are designed to allow light to pass through them but to prevent radiation from leaving them. Thus better thermal efficiencies can be achieved with this configuration due to less thermal losses.

Recently, nanoparticles (NPs) in dispersion in a base fluid have been used as the effective absorption media in Direct Absorption Solar Collectors (DASC) [7]. More precisely, remarkable photothermal conversion efficiency has been observed for gold [8–10] and silver [11–13] NPs owing to their surface plasmon resonance [11, 14]. Other non-metallic materials, such as carbon, are also used as NPs as well because they present good light absorbance throughout the solar spectrum [15].

This dispersion of nanoparticles in a base fluid receives the name of nanofluids [16], which are one of the technologies being investigated in DASC systems. Commonly, conventional base fluids (water and oils) are transparent, and hence, present low light absorption. For this reason, NPs are dispersed inside fluid to enhance the mixture's optical properties. Currently, a specific branch of nanofluids, solar nanofluids [17, 18], in which low concentrations of NPs absorb solar radiation, is being investigated for DASC applications. Further details of using nanofluids in solar collectors are reported in [15, 19–24].

Briefly, light-to-heat conversion in NPs may contribute to increase the efficiency of volumetric collectors, and presently constitutes an active research line. Yet, despite the fact that different nanoscale thermometry techniques are reported in the literature [25–27], the light-induced heat transfer of a single NP cannot be easily measured experimentally given the complexity of isolating a single NP and measuring the heat transfer

produced by light irradiation [28]. Therefore, numerical simulations can contribute to predict the temperature increase generated by the incident radiation on NPs and its surroundings to obtain the optimal solar nanofluid in volumetric collector applications.

Accordingly, the present work aims to state both theoretical and numerical formulations to study and understand light-to-heat energy conversion.

Light-to-heat conversion in NPs appears to be governed by the same physics that govern electromagnetic heating [29–31]. In this context, a sensible amount of the literature on light-to-heat conversion addresses the solution of this problem by adopting a frequency-domain approach, as is often the case with electrical engineering and telecommunication communities.

The expression of power dissipation,  $P_d$ , produced by light-to-heat in the frequency domain and usually found in the literature reads [29, 32–34]:

$$P_d = \frac{1}{2} \left[ \frac{\gamma}{\omega\epsilon_0} + \epsilon'' \right] \omega\epsilon_0 \left| \hat{E}_0 \right|^2, \quad (1)$$

where  $\gamma$ ,  $\omega$ ,  $\epsilon''$  and  $\left| \hat{E}_0 \right|$  denote electric conductivity, excitation pulsation, imaginary part of the complex relative permittivity and modulus of the complex amplitude of the sinusoidal electric field, respectively. Parameter  $\epsilon_0 = 8.854 \cdot 10^{-12}$  (F/m) is vacuum permittivity. Note that: i) this expression is valid only for sinusoidal excitations; ii) the term corresponding to Joule's dissipation [35] is often omitted from the literature but is added in the present work for the sake of completeness. In fact, equation (1) is the root mean square (RMS) value of the power dissipation for sinusoidal excitation and, consequently, provides a term-averaged dissipation instead of an instantaneous one.

Although both temporal and frequency domain approaches are valid, only one of both formalisms should be used for the sake of consistency in coupled problems. Consequently, the novelty of the present work lies in developing a thermodynamically consistent framework in the time domain from a multiphysics perspective to account for time-instantaneous dissipation. Therefore, the present formalism can be extended easily

to include more phenomena.

Three approaches exist in the literature to derive the source term in the energy balance responsible for light-to-heat conversion, often referred to as *power loss* term:

- The electrodynamic approach [34], which considers that the total current displacement stems from two different contributions: one due to the electric field and the other resulting from the remnant displacement current. The latter accounts for both partial energy storage in the medium and the power loss term behind microwave heating.
- The equivalent circuit approach [34], which is mainly used by the electric engineering community and establishes an analogy between the energy of an electric field and that of an electric circuit composed of capacitors and a resistor. The latter stands for the dissipation term in light-to-heat conversion.
- Non-equilibrium thermodynamic (NET) formalism, for which two different techniques can be contemplated:
  - The standard NET [36–38], based on the local equilibrium assumption and the formulation of the entropy balance to derive transport equations.
  - The hidden variable technique [39, 40], which consists of enlarging the set of thermodynamic variables of the problem to include further irreversible contributions in the formalism at the expense of increasing the number of phenomenological coefficients to be experimentally measured.

The standard NET approach is retained in this work; more precisely, the Debye model [41] is used to describe the source of irreversibilities associated with the time lag between polarisation and the electric field and, thus, responsible for light-to-heat conversion.

From a theoretical point of view, a robust thermodynamically consistent formulation based on both the Equilibrium Thermodynamics (ET) [42] and the NET formalisms is herein developed. In particular, the electric charge balance is obtained from Maxwell's

Mathematical operators	Description
$\dot{()}$	First time derivative
$\ddot{()}$	Second time derivative
$\underline{()}$	First-order tensor
$\underline{\underline{()}}$	Second-order tensor
$() \cdot ()$	Dot product

Table 1: Mathematical notation through the work.

laws and, afterwards, energy and entropy balances are stated to obtain transport (also called constitutive) equations.

In numerical terms, the set of two coupled partial differential equations is discretised in the Finite Element (FE) method [43]. Indeed, a three-dimensional, monolithic and non-linear formulation based on residuals is developed by using eight-noded brick elements with two degrees of freedom per node, namely voltage and temperature. Then the non-linearities due to quadratic dependence on the electric field are solved by the Newton-Raphson algorithm and the time integration by the standard Newmark- $\beta$  scheme.

Finally, the numerical formulation is implemented into the research code FEAP [44] and is validated against one-dimensional closed solutions. Then, a three-dimensional model of a single gold, a silver and a graphite nanoparticle (Au, Ag and G NP) is studied to demonstrate the capabilities of the present formulation for studying light-to-heat energy conversion.

The present work considers the following assumptions: i) NPs are poor light emitters, namely the quantity of light-induced heat in the NP is generated mainly by light absorption, as argued in [9]; ii) the scattering of incident light on NPs is negligible as long as the size of NPs is small compared to the incident light wavelength [45]; iii) lack of magnetic fields.

## 2. Theoretical formulation

For the theoretical formulation, a material that couples thermal and electrical energies and fills a body of domain  $\Omega$  and boundary  $\Gamma$ , with its outward normal  $\underline{n}$  is considered. Light-to-heat energy conversion is described by a set of two coupled differential equations, which are obtained from electromagnetism and thermodynamics formalisms. Table 1 summarises the mathematical notation used throughout.

### 2.1. Electromagnetism

Electromagnetism studies the interaction between electric  $\underline{E}$  and magnetic  $\underline{H}$  fields with their sources and is grounded on a set of four empirical equations called Maxwell's laws, from which the following two are needed to establish the present formalism:

$$\underline{\nabla} \times \underline{E} = -\dot{\underline{B}}, \quad \underline{\nabla} \times \underline{H} = \underline{j} + \dot{\underline{D}}. \quad (2)$$

From left to right, the first and second equations (Faraday's and Ampère's laws) relate the corresponding physical field to their vector sources: magnetic induction  $\underline{B}$ , free electric currents  $\underline{j}$  and electric displacement  $\underline{D}$ .

The electromagnetic formalism is completed by introducing three new equations, which can be directly obtained from (2):

- Despite the fact that the electric field may derive from either vectorial or scalar potentials, as argued in [46], the present work uses the scalar potential, –commonly called voltage–  $V$ . This potential is obtained by applying the fundamental theorem of vector calculus to Faraday's law of (2) when magnetic fields are absent:

$$\underline{\nabla} \times \underline{E} = 0 \Rightarrow \underline{E} = -\underline{\nabla}V. \quad (3)$$

- Polarisation vector  $\underline{P}$ , which takes into account the average of the electric dipolar

momentum in polarisable media, reads:

$$\underline{P} = \underline{D} - \epsilon_0 \underline{E}. \quad (4)$$

- The electric charge balance, which is obtained from Ampère's law and by using a vector calculus relation, which states that the divergence of the curl is always zero for any vector field:

$$\underline{\nabla} \cdot (\underline{j} + \dot{\underline{D}}) = 0. \quad (5)$$

Note that, despite term  $\dot{\underline{D}}$  often being called displacement current, its physical nature is not that of an electric current, but merely represents a time-varying electric field.

## 2.2. Thermodynamics

Within the continuum thermodynamics framework, light-to-heat energy conversion is a coupled interaction that deals with both reversible and irreversible processes; consequently, both ET and NET formalisms are herein used.

In this context, electric displacement is decomposed as the sum of its reversible (superscript  $r$ ) and irreversible (superscript  $i$ ) contributions:  $\underline{D} = \underline{D}^r + \underline{D}^i$ .

### 2.2.1. Equilibrium thermodynamics (ET)

Within the ET framework, the differential form of the energy balance reads:

$$d\mathcal{U} = Td\mathcal{S} + d\mathcal{W}, \quad (6)$$

where  $\mathcal{U}$ ,  $T$ ,  $\mathcal{S}$  and  $\mathcal{W}$  denote internal energy, temperature, entropy and work, respectively.

According to [46],  $d\mathcal{W}$  may be expressed as the product between intensive variable



$\underline{E}$  and its conjugate extensive variable  $\underline{D}^r$  so that (6) becomes:

$$d\mathcal{U}(S, \underline{D}^r) = T dS + \underline{E} \cdot d\underline{D}^r. \quad (7)$$

In order to obtain an amenable displacement-based FE formulation, a Legendre transformation is applied to (7) and the Gibbs-like energy  $\mathcal{G}$  becomes [47]:

$$d\mathcal{G}(T, \underline{E}) = -S dT - \underline{D}^r \cdot d\underline{E}. \quad (8)$$

In a first and good approximation, the explicit expression of  $\mathcal{G}(T, \underline{E})$  may be obtained by Taylor's expansion as in [46] to give:

$$\mathcal{G}(T, \underline{E}) = -\frac{1}{2} \underline{E} \cdot \underline{\epsilon}^r \cdot \underline{E} - C \left[ T \ln \left( \frac{T}{T_0} \right) - (T - T_0) \right], \quad (9)$$

where  $C$ ,  $T_0$  and  $\underline{\epsilon}^r$  denote heat capacity, reference temperature and the reversible part of the permittivity of the medium, respectively. Note that pyroelectric coupling is neglected in the present study.

Finally, the reversible constitutive equations are calculated from (8) and (9) by using standard ET procedures to give:

$$S = -\left. \frac{\partial \mathcal{G}(T, \underline{E})}{\partial T} \right|_{\underline{E}} = C \ln \left( \frac{T}{T_0} \right), \quad \underline{D}^r = -\left. \frac{\partial \mathcal{G}(T, \underline{E})}{\partial \underline{E}} \right|_T = \underline{\epsilon}^r \cdot \underline{E}. \quad (10)$$

### 2.2.2. Non-equilibrium thermodynamics (NET)

The NET formalism deals with irreversible processes and, consequently, the energy rate balance of (7) becomes:

$$\frac{d}{dt} \mathcal{U} = T \frac{d}{dt} S + \frac{d}{dt} (\mathcal{W}^r + \mathcal{W}^i), \quad (11)$$

where  $t$  denotes time. Furthermore, NET works with continuum equations and the three terms of (11) must be expressed in continuum forms:

- The term on the left-hand side of (11) reads:

$$\frac{d}{dt}\mathcal{U} = \int_{\Omega} \rho \dot{u} d\Omega, \quad (12)$$

where  $\rho$  and  $\dot{u}$  denote mass density and the specific internal energy rate, respectively.

- The first term on the right-hand side of (11) may be expressed in a continuum form by introducing heat flux  $\underline{q}$  to give:

$$T \frac{d}{dt}\mathcal{S} = - \int_{\Gamma} \underline{q} \cdot \underline{n} d\Gamma = - \int_{\Omega} \underline{\nabla} \cdot \underline{q} d\Omega, \quad (13)$$

where the divergence theorem has been used. Note that this equation represents the reversible entropy, which is the heat flux exchanged through the boundary  $\Gamma$ .

- The second term on the right-hand side of (11) becomes:

$$\frac{d}{dt}(\mathcal{W}^r + \mathcal{W}^i) = - \int_{\Gamma} \underline{S} \cdot \underline{n} d\Gamma + \int_{\Omega} r d\Omega, \quad (14)$$

where  $\underline{S} = \underline{E} \times \underline{H}$  is the Poynting vector and  $r$  is the heat source/sink term. By applying the divergence theorem to the term on the right-hand side of (14) and taking into account the vector identity  $\underline{\nabla} \cdot (\underline{E} \times \underline{H}) = \underline{H} \cdot (\underline{\nabla} \times \underline{E}) - \underline{E} \cdot (\underline{\nabla} \times \underline{H})$  and Ampère's law of (2), the electromagnetic power, the first term on the right-hand side of (14), reads when magnetic field is absent:

$$\int_{\Gamma} \underline{S} \cdot \underline{n} d\Gamma = - \int_{\Omega} [\underline{j} \cdot \underline{E} + \underline{\dot{D}} \cdot \underline{E}] d\Omega. \quad (15)$$

As observed, the reversible power is given by  $\underline{\dot{D}}^r \cdot \underline{E}$ , while the irreversible one is due to two contributions: Joule's heating, mathematically represented by  $\underline{j} \cdot \underline{E}$ , and polarisation heating,  $\underline{\dot{D}}^i \cdot \underline{E}$ .

By combining (15), (14), (13), (12) and (11), the NET energy balance when magnetic

fields are lacking becomes:

$$\int_{\Omega} \rho \dot{u} \, d\Omega = - \int_{\Omega} \left( \underline{\nabla} \cdot \underline{q} - \underline{j} \cdot \underline{E} - \underline{\dot{D}} \cdot \underline{E} - r \right) \, d\Omega. \quad (16)$$

The energy balance is expressed in terms of temperature for its numerical implementation by substituting the rate of (7) and (10) (left) into (16):

$$\int_{\Omega} \rho c \dot{T} \, d\Omega = - \int_{\Omega} \underline{\nabla} \cdot \underline{q} \, d\Omega + \int_{\Omega} \left( \underline{j} + \underline{\dot{D}}^i \right) \cdot \underline{E} \, d\Omega + \int_{\Omega} r \, d\Omega, \quad (17)$$

where  $c$  represents the specific heat capacity.

At this point, the entropy balance must be calculated to obtain the material constitution. For this purpose, the reversible energy rate given in (7) is inserted into (16) to obtain:

$$\int_{\Omega} \rho \dot{s} \, d\Omega = - \int_{\Omega} \underline{\nabla} \cdot \left( \frac{\underline{q}}{T} \right) \, d\Omega + \int_{\Omega} \left[ -\underline{q} \cdot \left( \frac{\underline{\nabla} T}{T^2} \right) + \frac{\underline{j} \cdot \underline{E}}{T} + \frac{\underline{\dot{D}}^i \cdot \underline{E}}{T} + \frac{r}{T} \right] \, d\Omega, \quad (18)$$

where  $s$  refers to specific entropy and the chain rule is used for convenience to rewrite the heat flux term.

According to [36, 37], the entropy balance in the NET context reads:

$$\int_{\Omega} \rho \dot{s} \, d\Omega = - \int_{\Omega} \underline{\nabla} \cdot \underline{j}_s \, d\Omega + \int_{\Omega} \sigma_s \, d\Omega, \quad (19)$$

consequently, by comparing (18) and (19), entropy flux  $\underline{j}_s$  and entropy production  $\sigma_s$  may be explicitly expressed as:

$$\underline{j}_s = \frac{\underline{q}}{T}, \quad \sigma_s = -\underline{q} \cdot \left( \frac{\underline{\nabla} T}{T^2} \right) + \frac{\underline{j} \cdot \underline{E}}{T} + \frac{\underline{\dot{D}}^i \cdot \underline{E}}{T} + \frac{r}{T} \geq 0. \quad (20)$$

From  $\sigma_s$  of (20), it is concluded that entropy sources are due to three irreversible processes:

- Heat conduction, the first term on the right-hand side of the second equation
- Joule's heating, the second term
- Polarisation heating, the third term

Finally, to obtain the material constitution (known as transport equations in the NET context), the entropy production of (20) may be expressed in a first good and reasonable approximation as a linear combination of fluxes and driving forces [36, 37]:

$$\underline{j} = \underline{\underline{\gamma}} \cdot \underline{E}, \quad \underline{q} = -\underline{\underline{\kappa}} \cdot \nabla T, \quad \dot{\underline{D}}^i = \underline{\underline{\epsilon}}^i \cdot \ddot{\underline{E}}, \quad (21)$$

where  $\underline{\underline{\gamma}}$  and  $\underline{\underline{\kappa}}$  denote electrical and thermal conductivity, respectively. Coefficient  $\underline{\underline{\epsilon}}^i$  represents the irreversible part of the permittivity of the medium. This irreversible permittivity depends on  $\epsilon_s$  and  $\epsilon_\infty$ , which are known as static and high-frequency relative permittivity, respectively. In turn these two parameters are directly related to complex relative permittivity  $\epsilon_r(\lambda)$ , which is the measurement generally provided in the material databases. The relation among  $\epsilon_s$ ,  $\epsilon_\infty$  and  $\epsilon_r(\lambda)$  is explicitly reported in Appendix A. The detail of the derivation of the Debye relaxation law in the time domain in (21) (right) and the definition of  $\underline{\underline{\epsilon}}^r$  and  $\underline{\underline{\epsilon}}^i$  are explicitly reported in Appendix B.

Solving coupled physical phenomena of different nature in a numerical and monolithic approach, which is the intention of this work, could lead to accuracy issues given the very different orders of magnitude of the involved physical quantities. Some numerical problems regarding accuracy arise in the present formulation if (21) (right) is directly used. Therefore, for the sake of numerical accuracy, this equation is re-expressed to avoid such errors.

As the excitation electric field is assumed to be harmonic, the following relation between the electric field and its second-time derivative holds:

$$\ddot{\underline{E}} = -\omega^2 \underline{E}. \quad (22)$$

By substituting (22) in (21) (right), the Debye relaxation law can be re-expressed as:

$$\dot{\underline{D}}^i = -\omega^2 \underline{\underline{\epsilon}}^i \cdot \underline{E} = \underline{\underline{\epsilon}}^{i*} \cdot \underline{E}, \quad (23)$$

where the new coefficient  $\underline{\underline{\epsilon}}^{i*}$  is defined for the sake of compactness in the notation as:

$$\underline{\underline{\epsilon}}^{i*} = \epsilon_0 \frac{\epsilon_s - \epsilon_\infty}{1 + \omega^2 \tau^2} \tau \omega^2 \underline{I}, \quad (24)$$

where  $\underline{I}$  is the identity tensor.

Hence, equation (23) proves more convenient numerically and will be henceforth used even though, in essence, both (21) (right) and (23) describe the same physical phenomenon.

### 2.3. Boundary conditions

The boundary conditions for the two degrees of freedom, namely  $T$  and  $V$ , are composed of Dirichlet and Neumann expressions:

$$\text{Dirichlet:} \quad T = \bar{T}, \quad V = \bar{V}, \quad (25)$$

$$\text{Neumann:} \quad \underline{q} \cdot \underline{n} = \bar{q}, \quad \underline{j} \cdot \underline{n} = \bar{j}, \quad \underline{D} \cdot \underline{n} = \bar{D},$$

where  $\bar{T}$ ,  $\bar{V}$ ,  $\bar{q}$ ,  $\bar{j}$  and  $\bar{D}$  are the prescribed temperature, voltage, thermal flux, electric flux and electric displacement, respectively.

## 3. Finite element formulation

This section presents a variational approach in the FE context [43] to numerically express the governing equations of light-to-heat conversion. For this purpose: i) the balance equations are multiplied by test functions; ii) isoparametric discretisations are introduced; iii) a residual-based formulation is obtained to solve the problem's non-

linearity (thermal sources quadratically depend on the electric field); iv) tangent matrices are calculated.

### 3.1. Weak forms

As previously mentioned, weak forms are obtained by multiplying (5) and (17) by test functions  $(\delta T, \delta V)$  respectively, and by applying the divergence theorem and introducing the Neumann boundary conditions of (25):

$$\begin{aligned} \int_{\Omega} \underline{\nabla} \delta T \cdot \underline{q} \, d\Omega - \int_{\Omega} \delta T \rho c \dot{T} \, d\Omega - \int_{\Gamma} \delta T \underline{q} \cdot \underline{n} \, d\Gamma + \int_{\Omega} \delta T (\underline{j} + \underline{\dot{D}}^i) \cdot \underline{E} \, d\Omega \\ + \int_{\Omega} \delta T r \, d\Omega = 0, \end{aligned} \quad (26)$$

$$\int_{\Omega} \underline{\nabla} \delta V \cdot (\underline{j} + \underline{\dot{D}}) \, d\Omega - \int_{\Gamma} \delta V (\underline{j} + \underline{\dot{D}}) \cdot \underline{n} \, d\Gamma = 0.$$

### 3.2. Discretisations

At this point, continuum domain  $\Omega$  with boundary  $\Gamma$  is discretised by using  $n$  elements of domain  $\Omega_e$  and boundary  $\Gamma_e$ . For this purpose, the present work uses eight-noded brick elements with standard Lagrange-type shape functions  $\mathcal{N}$  to interpolate the degrees of freedom and spatial coordinates.

$$T \approx \mathcal{N}_b a_b^T, \quad \delta T \approx \mathcal{N}_b \delta a_b^T, \quad \underline{\nabla} T \approx \underline{\mathcal{B}}_b a_b^T, \quad \underline{\nabla} \delta T \approx \underline{\mathcal{B}}_b \delta a_b^T, \quad (27)$$

$$V \approx \mathcal{N}_b a_b^V, \quad \delta V \approx \mathcal{N}_b \delta a_b^V, \quad \underline{\nabla} V \approx \underline{\mathcal{B}}_b a_b^V, \quad \underline{\nabla} \delta V \approx \underline{\mathcal{B}}_b \delta a_b^V,$$

where the Einstein summation convention is used,  $\underline{\mathcal{B}}$  represents the shape function gradient matrix, and  $a_b^j$  denotes the nodal values in a generic node  $b$  for each degree of freedom  $j = \{T, V\}$ .

### 3.3. Residuals

The discretisations of (27) are introduced into (26) to obtain the residuals in a generic node  $a$ :

$$\begin{aligned} \mathcal{R}_a^T &= \int_{\Omega_e} \underline{\mathcal{B}}_a \underline{q} \, d\Omega_e - \int_{\Omega_e} \mathcal{N}_a \rho c \mathcal{N}_i \dot{a}_i^T \, d\Omega_e - \int_{\Gamma_e} \mathcal{N}_a \underline{q} \underline{n} \, d\Gamma_e \\ &\quad - \int_{\Omega_e} \mathcal{N}_a \left( \underline{j} + \underline{\dot{D}}^i \right) \cdot \underline{\mathcal{B}}_i a_i^V \, d\Omega_e + \int_{\Omega_e} \mathcal{N}_a r \, d\Omega_e, \end{aligned} \quad (28)$$

$$\mathcal{R}_a^V = \int_{\Omega_e} \underline{\mathcal{B}}_a \cdot \left( \underline{j} + \underline{\dot{D}} \right) \, d\Omega_e - \int_{\Gamma_e} \mathcal{N}_a \left( \underline{j} + \underline{\dot{D}} \right) \cdot \underline{n} \, d\Gamma_e,$$

where  $\underline{q} = -\underline{\kappa} \cdot \underline{\mathcal{B}}_i a_i^T$ ,  $\underline{j} = -\underline{\gamma} \cdot \underline{\mathcal{B}}_i a_i^V$  and  $\underline{\dot{D}} = \underline{\dot{D}}^r + \underline{\dot{D}}^i$ , where  $\underline{\dot{D}}^r = -\underline{\epsilon}^r \cdot \underline{\mathcal{B}}_i a_i^V$  and  $\underline{\dot{D}}^i = -\underline{\epsilon}^{i*} \cdot \underline{\mathcal{B}}_i a_i^V$ .

### 3.4. Tangent matrices

Tangent matrices are obtained by standard FE procedures:

$$\mathcal{K}_{ab}^{ij} = -\frac{\partial \mathcal{R}_a^i}{\partial a_b^j}, \quad \mathcal{C}_{ab}^{ij} = -\frac{\partial \mathcal{R}_a^i}{\partial \dot{a}_b^j}, \quad \mathcal{M}_{ab}^{ij} = -\frac{\partial \mathcal{R}_a^i}{\partial \ddot{a}_b^j}, \quad (29)$$

where  $\mathcal{K}$ ,  $\mathcal{C}$  and  $\mathcal{M}$  denote the tangent stiffness, capacity and mass matrices, respectively. Indices  $i$  and  $j$  refer to degrees of freedom and  $a$  and  $b$  to two generic nodes.

For the sake of clarity, tangent matrices are explicitly reported in Appendix C. Finally, the monolithic assembled matrix becomes:

$$\begin{bmatrix} \mathcal{K}_{ab}^{TT} + c_2 \mathcal{C}_{ab}^{TT} & \mathcal{K}_{ab}^{TV} \\ 0 & \mathcal{K}_{ab}^{VV} + c_2 \mathcal{C}_{ab}^{VV} \end{bmatrix} \begin{Bmatrix} da_b^T \\ da_b^V \end{Bmatrix} = \begin{Bmatrix} \mathcal{R}_b^T \\ \mathcal{R}_b^V \end{Bmatrix}, \quad (30)$$

where coefficient  $c_2$  is a scalar involving the parameters of the time integration scheme as reported in [48].

The present FE formulation is implemented into the research code **FEAP** [48], which belongs to the University of California at Berkeley (USA). This software holds *dummy* subroutines to add elements, while non-linear solvers and time integration algorithms are already implemented. In particular, the present work uses the standard Newton-Raphson algorithm to solve non-linearities and backward differences for the time integration.

#### 4. Results

This section presents a validation of the present formulation to ensure proper implementation and, in addition, several study scenarios are presented to provide profounder physical insight into the comprehension of light-to-heat conversion in solar nanofluids.

##### 4.1. One-dimensional validation

In this section, the numerical code is compared to a simple one-dimensional, time-independent excitation and steady-state analytical solution developed by the authors and reported in Appendix D. The one-dimensional domain and its boundary conditions are shown in Figure 1:

- The length of the domain is  $L = 0.1$  (m).
- $T_1 = 303.15$  (K) and  $V_1 = 0$  (V) denote prescribed values on the left-end.
- $T_2 = 353.15$  (K) and  $V_2 = \{0.05, 0.1, 0.2\}$  (V) on the right-end.

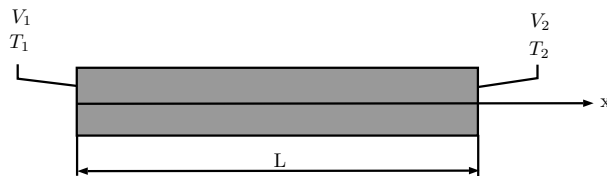


Figure 1: Geometry and boundary conditions of the one-dimensional domain used for the validation of the numerical model.

For the validation, gold (Au) is considered because it is one of the most frequently used materials for light-to-heat conversion in NPs. The material properties of Au are obtained



from [49–53] and summarised in Table 2. Note that the relative permittivity values  $\epsilon_r(\lambda) = \epsilon/\epsilon_0$  provided in Table 2 are expressed in complex form, as in the literature, at a wavelength  $\lambda = 400$  (nm) and  $i$  represents the imaginary unit.

Material	Properties	Value	Units
Gold (Au)	$\rho$	19320	kg/m <sup>3</sup>
	$c$	131.4	J/(kg · K)
	$\kappa$	312	W/(m · K)
	$\gamma$	$3.17 \cdot 10^7$	( $\Omega \cdot \text{m}$ ) <sup>-1</sup>
	$\epsilon_r(\lambda)$	$-1.4421 - 6.3962 i$	-
	$n(\lambda)$	$1.5992 + 1.9998 i$	-
Silver (Ag)	$\rho$	10490	kg/m <sup>3</sup>
	$c$	240.49	J/(kg · K)
	$\kappa$	420	W/(m · K)
	$\gamma$	$4.42 \cdot 10^7$	( $\Omega \cdot \text{m}$ ) <sup>-1</sup>
	$\epsilon_r(\lambda)$	$-3.3668 - 0.7122 i$	-
	$n(\lambda)$	$0.1930 + 1.8450 i$	-
Graphite (G)	$\rho$	2100	kg/m <sup>3</sup>
	$c$	1041.36	J/(kg · K)
	$\kappa$	390	W/(m · K)
	$\gamma$	$2 \cdot 10^3$	( $\Omega \cdot \text{m}$ ) <sup>-1</sup>
	$\epsilon_r(\lambda)$	$2.2285 - 3.1024 i$	-
	$n(\lambda)$	$1.7390 + 0.8920 i$	-
Water (H <sub>2</sub> O)	$\rho$	988.037	kg/m <sup>3</sup>
	$c$	4176.84	J/(kg · K)
	$\kappa$	0.645	W/(m · K)
	$\gamma$	$5.5 \cdot 10^{-6}$	( $\Omega \cdot \text{m}$ ) <sup>-1</sup>
	$\epsilon_r(\lambda)$	$1.7929 - 5 \cdot 10^{-9} i$	-
	$n(\lambda)$	$1.3390 + 1.9 \cdot 10^{-9} i$	-

Table 2: Material properties for different materials.

Figure 2 compares the analytical (solid lines) and numerical solutions (solid circles) for  $T$  and  $V$  distributions in the study domain. As observed, an excellent agreement is reached between the analytical and numerical solutions for this simple validation; the

maximum relative error is 0.0014 (%). In addition, the non-linearity due to the quadratic dependence of Joule's heating is solved by 3 iterations of the Newton-Raphson algorithm. This non-linearity can be observed in the quadratic distribution of temperature shown in Figure 2 (left).

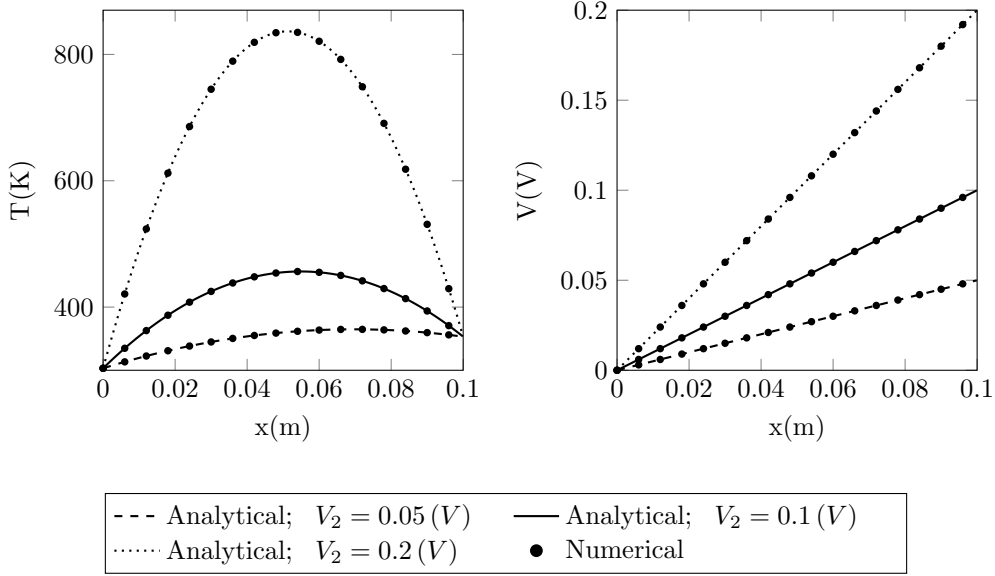


Figure 2: Comparison of the steady-state analytical and numerical distributions of temperature (left) and voltage (right) along the one-dimensional domain shown in Figure 1 for three different values of prescribed voltage  $V_2 = \{0.05, 0.1, 0.2\}$  (V) at the right end of the geometry.

#### 4.2. Three-dimensional simulation

This section presents a three-dimensional simulation of an Au NP surrounded by water and irradiated by a laser beam to determine the instantaneous heat dissipation in the surroundings of a single NP. Figure 3 shows the domain with its boundary conditions: the voltage reference is set at  $V_0 = 0$  (V) at  $x = L/2$  and a time-dependent voltage  $V(t) = V_0 \sin(\omega t)$ , with  $V_0$  denoting voltage amplitude, is prescribed at  $x = -L/2$ . Temperature boundary conditions are set at a constant fixed value for each side of the cube in Figure 3. The centre of the NP is located at the origin of the reference system.

The Au NP is excited by a laser beam at 400 (nm) and amplitude  $V_0$  is computed

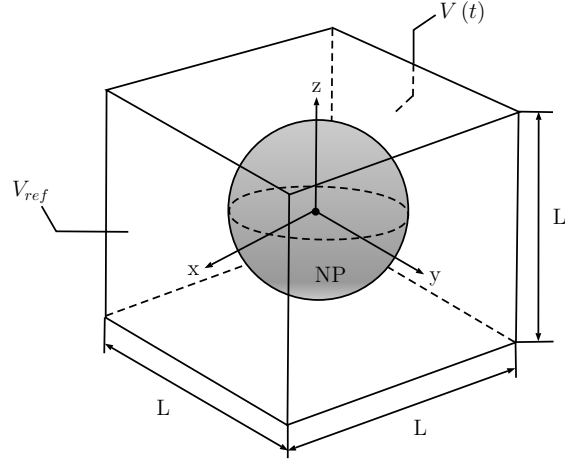


Figure 3: Geometry and boundary conditions of the three-dimensional simulation.

from the definition of the RMS value of laser intensity ([9]) as follows:

$$V_0 = \sqrt{\frac{2I_{laser}}{c_{light} \epsilon_0 \|n_{H_2O}(\lambda)\|}} L, \quad (31)$$

where  $I_{laser}$ ,  $c_{light}$  and  $\|n_{H_2O}(\lambda)\|$  denote the RMS value of the laser flux, speed of light and the norm of the wavelength-dependent complex refractive index of water, respectively. Note that the laser flux considered for the simulations is obtained from the literature [9]:  $I_{laser} = 5 \times 10^4$  (W/cm<sup>2</sup>).

Excitation pulsation  $\omega$  can be determined from wavelength  $\lambda$  of incident excitation as follows:

$$\omega = \frac{2\pi c_{light}}{\lambda \|n(\lambda)\|}, \quad (32)$$

where  $\|n(\lambda)\|$  denotes the norm of the complex refractive index.

For the sake of completeness for the parameter calibration in the present model, relaxation time  $\tau$  is necessary for the Debye law and is computed as follows ([54]):

$$\tau = \frac{\lambda_c \|n(\lambda_c)\|}{2\pi c_{light}}, \quad (33)$$

where subscript  $c$  denotes the critical point in the wavelength spectrum at which the relaxation phenomenon occurs. According to [55], this critical point can be determined as the intersection between the real and imaginary part functions of the complex relative permittivity. Once the critical point is found, the optical material properties at the critical wavelength such as the refractive index can be determined.

For the geometrical dimensions, the diameter of the Au NP is 20 (nm) and the length of the surrounding medium, controlled by  $L$ , is chosen to be large enough to avoid edge effects. For this first study,  $L$  is taken to be 10-fold bigger than the diameter of the NP. Finally, the material properties of gold and water, which are obtained from [49, 53, 56, 57] for water, are reported in Table 2.

The increase in temperature, namely, light-to-heat conversion, is shown in Figure 4 for the different sinusoidal excitation function values at four different times. As expected, the parabolic temperature increase profiles are obtained around the NPs, where the maximum temperature increase is reached at the centre of the NP and is directly proportional to the amplitude of the prescribed voltage. Note also that although sinusoidal excitation may take negative values as in Figure 4, as the dissipation due to polarisation phenomena responds to a quadratic effect, the sinusoidal excitation sign has no influence on dissipation.

For dissipation terms in the energy balance (17), two main terms contribute to light-to-heat conversion: Joule's and polarisation effects. The former is governed by the material's electrical conductivity, and the latter by the irreversible part of relative permittivity.

Concerning Joule's heating, this source is relevant for low-frequency excitations, but not for high-frequencies, which are those at which light-to-heat conversion takes place; at approximately 560 (THz) for the simulations presented in this Section. Note that electrostatics can be approximated to quasi-static phenomena until frequency of the order of 10 (GHz) or lower is reached, as indicated in [58].

Regarding polarisation heating and by considering high-frequencies, it is numerically

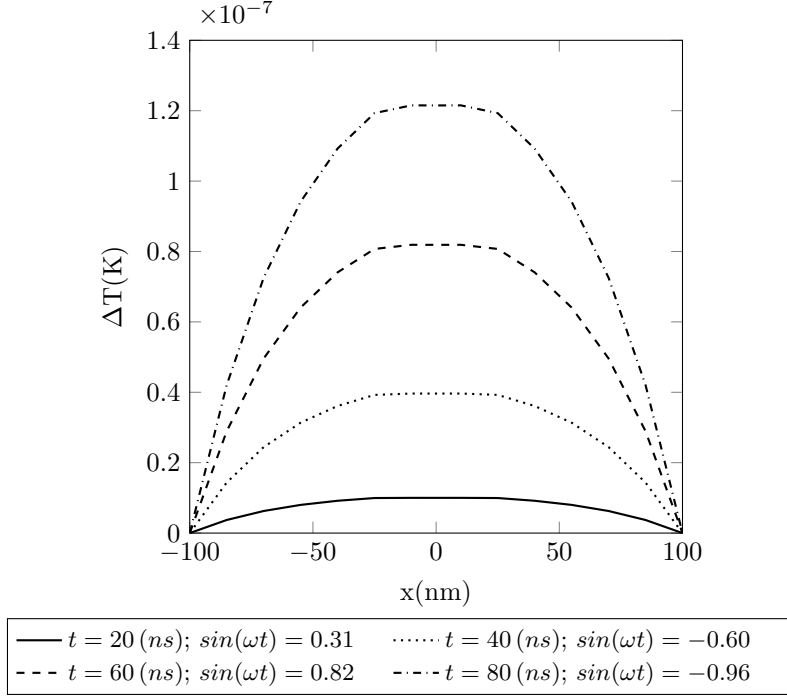


Figure 4: Temperature increase across the diameter of a gold nanoparticle centred at  $x = 0$  (see Figure 3) for four different values of amplitude of sinusoidal excitation  $\sin(\omega t) = \{0.31, -0.60, 0.82, -0.96\}$  at four different times  $t = \{20, 40, 60, 80\}$  (ns). The nanoparticle is 20 (nm) in diameter and is irradiated by a laser flux of  $5 \times 10^4$  (W/cm<sup>2</sup>) at a wavelength  $\lambda = 400$  (nm).

verified that the temperature increase produced by Joule’s heating is much lower than that generated by polarisation heating. Therefore, the effects of Joule’s heating are included in the theoretical formulation for the sake of framework’s generality but are omitted from the subsequent examples to study light-to-heat conversion in NPs.

#### 4.3. Light-to-heat conversion for different NPs

This section compares heating in nanofluids due to the light-to-heat conversion for different materials used as NPs; namely gold (Au), silver (Ag) and graphite (G). The properties of Ag are taken from [49–51, 53, 59] and those of G are obtained from [49, 53, 60, 61]. Both are reported in Table 2 along with properties of Au and H<sub>2</sub>O.

Studying a model that considers fluid dynamics is beyond the scope of the present work. However, the model introduced in this work (see Figure 3) permits the simulation

of the medium surrounding a NP. Similarly, by considering that the surrounding medium (or base fluid in the nanofluids context) can be assumed to behave as a liquid at rest, this model can be used to simulate light-to-heat in nanofluids. Hence different concentrations of NPs in suspension in the base fluid can be reproduced by varying the volume ratio of the sphere representing the NP and the cube representing the base fluid. Hence volumetric concentration  $\phi$  used henceforth in this work is defined as follows:

$$\phi = \frac{v_{sphere}}{v_{cube}}, \quad (34)$$

where  $v_{sphere}$  and  $v_{cube}$  represent the volume of the sphere and the cube of our model, respectively.

Figure 5 shows the progressive temperature increase with time for water only, and for the Au, Ag and G NPs dispersed in water, to compare the different evolution of temperature increase of nanofluids. Note that the diameter considered for the simulation of the different NPs is 20 (nm). Four different concentration values are retained:  $\phi = \{0.0034, 0.0065, 0.016, 0.052\}$  (%) and, as experimentally confirmed, temperature increase is related to the concentration of the NPs in the base fluid.

Unlike the simulation presented in Section 4.2, the boundary conditions on temperature are not set at a fixed constant value, but are left unconstrained so that the temperature increase in the surrounding medium (water) can evolve with time. Note also that a unitary sinusoidal amplitude value is adopted for the simulations in this Section and that temperature increase is predicted on the outer surface of the NP that comes into contact with the base fluid.

Figure 5 depicts that for an excitation wavelength  $\lambda = 400$  (nm), the temperature increase numerically predicted for the Ag NPs is greater than that for G NPs, and the latter is still larger than that predicted for the Au NPs. This trend coincides with the literature [62–65] because for  $\lambda = 400$  (nm), the absorption coefficient (directly related to light-to-heat conversion) of the Ag NPs dispersed in water is higher than that of the G and Au NPs dispersed in water. This heating enhancement in the Ag NPs versus the

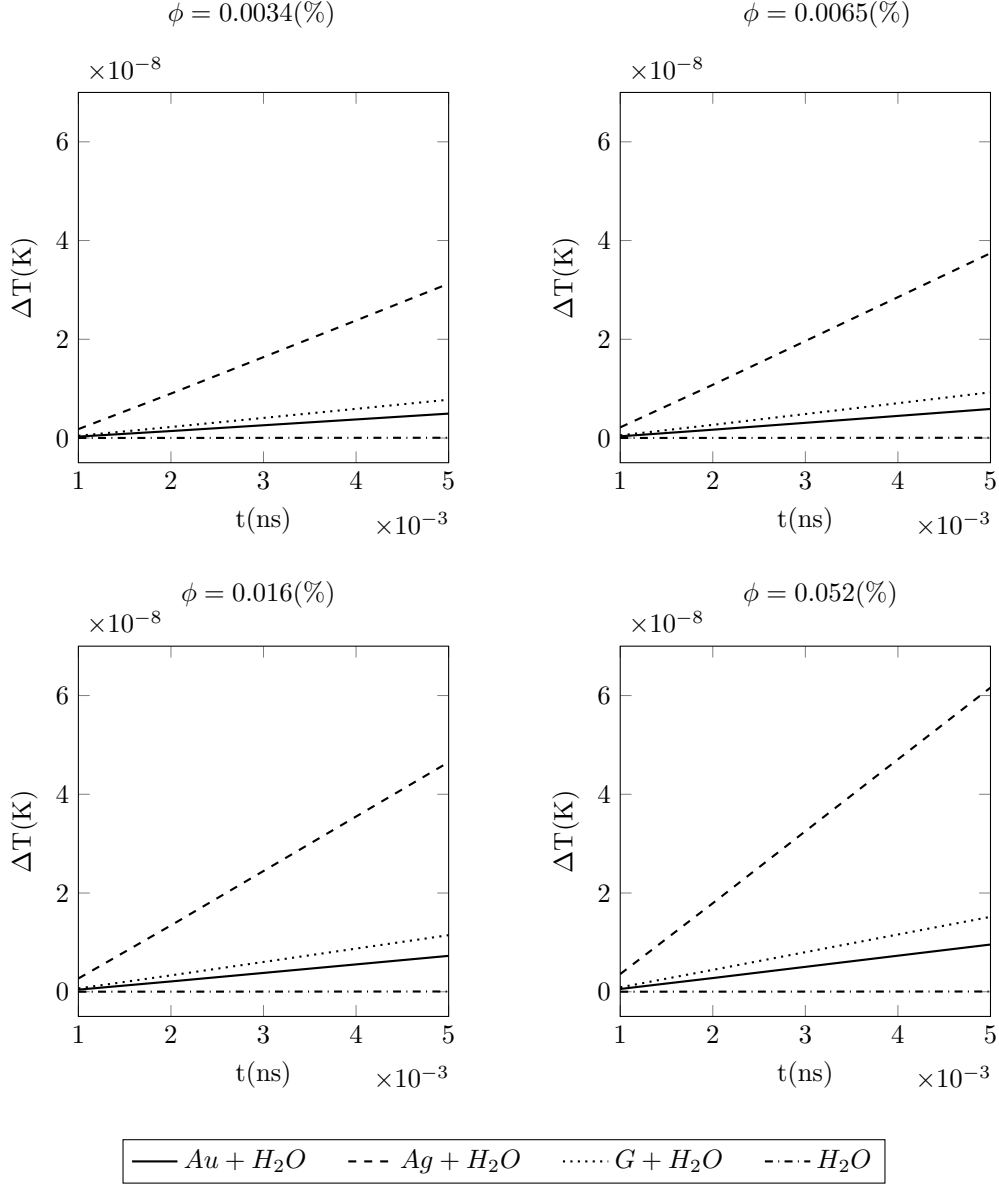


Figure 5: Time evolution of the temperature increase of different nanofluids for a laser flux  $I_{laser} = 5 \times 10^4$  (W/cm<sup>2</sup>) at a wavelength  $\lambda = 400$  (nm) for four different volumetric concentrations  $\phi = \{0.0034, 0.0065, 0.016, 0.052\}$  (%). The media considered for simulation are only water ( $H_2O$ ) and three different nanofluids composed of: gold nanoparticles dispersed in water ( $Au + H_2O$ ), silver nanoparticles dispersed in water ( $Ag + H_2O$ ) and graphite nanoparticles dispersed in water ( $G + H_2O$ ).

other NPs occurs because they are irradiated with an excitation wavelength  $\lambda = 400$  (nm), which matches the surface plasmon resonance of Ag.

#### 4.4. Evolution of temperature increase with concentration

This section presents a study on the influence of concentration on the temperature increase of nanofluids. For this purpose, a new metric that eliminates the effect of heating of the base fluid (water in this case) is defined in line with the dimensionless temperature increase below:

$$\Delta T_{dl} = \frac{\frac{\Delta T_{NF}}{\Delta t_{NF}}}{\frac{\Delta T_{H_2O}}{\Delta t_{H_2O}}}, \quad (35)$$

where the numerator in (35) represents the slope of the temperature increase in the nanofluid and the denominator denotes the slope of the temperature increase in the base fluid.

Several numerical simulations are performed for different nanofluids, namely Au, Ag and G NPs in suspension in water, to assess the influence of different volumetric concentrations on the predicted temperature increase. Figure 6 shows this evolution.

The trend observed in Figure 6 is that the higher the NPs concentration in the nanofluid, the more marked the predicted temperature increase. However in real applications, increasing the NPs concentration is not exempt of drawbacks as such a choice entails an upsurge in viscosity [66] and, consequently, more difficulty to pump the nanofluid in flow system applications. Another inconvenience of incrementing concentration is that the colloidal stability of the nanofluid is not guaranteed [67, 68], thus it is more likely to precipitate and then lose the working principle of the nanofluid. Moreover, continuously increasing the NPs concentration in the base fluid does not guarantee better light absorption as light-to-heat conversion is limited to top layers in solar nanofluids with high NPs concentrations [69].

Therefore, Figure 6 can be used by the experimental community to select the most convenient combination of NPs and their concentration for a desired application.



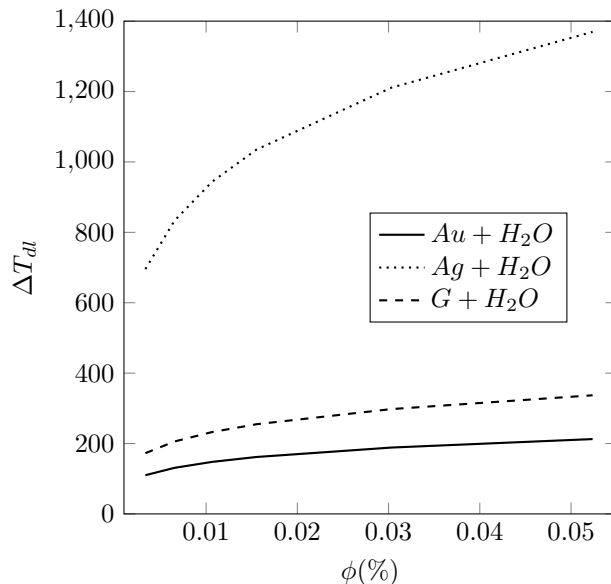


Figure 6: Evolution of the dimensionless temperature increase in relation to the volumetric concentration of the NPs in the nanofluid for three different nanofluids composed of: gold nanoparticles dispersed in water ( $Au + H_2O$ ), silver nanoparticles dispersed in water ( $Ag + H_2O$ ) and graphite nanoparticles dispersed in water ( $G + H_2O$ ) for a laser flux  $I_{laser} = 5 \times 10^4$  ( $W/cm^2$ ) at a wavelength  $\lambda = 400$  (nm).

## 5. Conclusions

This article presents a non-linear, three-dimensional, dynamic and thermodynamically consistent formulation applied to light-to-heat conversion for optically excited NPs. Theoretically, equilibrium and non-equilibrium thermodynamic formalisms are used to obtain the set of two coupled governing equations. Numerically, a finite element formulation for a light-to-heat problem is developed by using residuals due to the problems' non-linearities. Note that heat sources quadratically depend on the electric field. Finally, the numerical formulation is coded in a research software, is validated against a one-dimensional simulation and is used to perform several studies on light-to-heat conversion in solar nanofluids.

A good agreement is reached between the one-dimensional analytical solution and the numerical results, which permits to validate the present formulation. Furthermore, different numerical analyses are conducted for light-to-heat conversion in solar nano-

fluids. Firstly, the temperature increase around a single Au NP is obtained to verify the parabolic distribution of temperature for the different sinusoidal excitation values of a laser. Afterwards, the time evolution of the temperature increase for water and three different nanofluids is analysed: Au NPs dispersed in water, Ag NPs dispersed in water and graphite (G) NPs dispersed in water. The numerical simulations predict a major heating enhancement for the Ag NPs than for the G and Au NPs, respectively, which agrees with the experimental trends when these nanofluids are excited at a wavelength of 400 (nm) because this wavelength matches the surface plasmon resonance of Ag. Finally, a study on the influence of NP concentration in nanofluids is performed. It is concluded that the temperature increase due to light-to-heat conversion depends on the charge of NPs in the nanofluids but the concentration cannot be increased indefinitely as other practical issues, such as the lack of stability, the incremented viscosity of the nanofluid or the limitation of light absorption to top nanofluid layers become apparent.

In short, this numerical model can be used as a virtual laboratory to better understand the physical phenomena involved in light-to-heat conversion in NPs due to the complexity of measuring the temperature increase in a single NP from an experimental point of view. Therefore, this numerical tool can be used to make predictions to help select a certain combination of base fluid, NPs and their concentration in the nanofluid for a desired application by reducing the number of experiments to be conducted and consequently their cost.

## **Acknowledgements**

This research was partially funded by *Ministerio de Economía y Competitividad (MINECO)* of Spain through the project ENE2016-77694-R. Josep Forner-Escrig thanks *Ministerio de Ciencia, Innovación y Universidades* of Spain and Fondo Social Europeo for a pre-doctoral fellowship through Grant Ref. BES-2017-080217 (FPI programme). This work is developed by participants of the COST Action CA15119 Overcoming Barriers to Nanofluids Market Uptake (NANOUP TAKE). A special mention is made to J.

Enrique Juliá as a token of gratitude for inspiring the present work.

## Appendix A. Static and high-frequency relative permittivity

This appendix provides the relation between the measured complex relative permittivity  $\epsilon_r(\lambda)$  and parameters  $\epsilon_s$  and  $\epsilon_\infty$ , used in the present work for the Debye relaxation model.

Pulsation-dependent relative permittivity can be written in the form of a complex number:

$$\epsilon_r(\lambda) = \epsilon' + i\epsilon'', \quad (\text{A.1})$$

where  $\epsilon'$  and  $\epsilon''$  denote the real and imaginary part of complex permittivity, respectively.

The real and imaginary parts of complex relative permittivity in (B.1) are separated and the obtained expression is:

$$\epsilon_r(\lambda) = \epsilon_\infty + \frac{\epsilon_s - \epsilon_\infty}{1 + \omega^2\tau^2} - \frac{(\epsilon_s - \epsilon_\infty)i\omega\tau}{1 + \omega^2\tau^2}, \quad (\text{A.2})$$

where  $\tau$  represents the relaxation time.

By equalling the real and imaginary parts from (A.1) and (A.2), explicit algebraic expressions of  $\epsilon_s$  and  $\epsilon_\infty$  are obtained in terms of the experimentally measured coefficients:

$$\epsilon_s = \epsilon' - \epsilon''\omega\tau, \quad \epsilon_\infty = \epsilon' + \frac{\epsilon''}{\omega\tau}. \quad (\text{A.3})$$

## Appendix B. Debye relaxation law

The Debye relaxation law is usually provided in the frequency domain in literature [33, 34, 70] as follows:

$$\underline{D}(\omega) = \epsilon_0 \left( \epsilon_\infty + \frac{\epsilon_s - \epsilon_\infty}{1 + i\omega\tau} \right) \underline{I} \cdot \underline{E}(\omega). \quad (\text{B.1})$$

As a multiphysics time domain formulation is intended in the present work, and as the electric-field excitation is assumed to be monochromatic and harmonic to behave like a laser, the Debye relaxation model can be re-expressed analytically in the time domain by the inverse Fourier transform. More specifically, the following transforms are needed:

i) Rational function of pulsation

$$\frac{1}{2\pi} \int_{-\infty}^{+\infty} \frac{1}{a + i\omega} e^{i\omega t} d\omega = e^{-at} h(t), \quad (\text{B.2})$$

where  $a$  is a constant so that  $Re(a) > 0$  and  $h(t)$  represents the Heaviside step function.

ii) Convolution in time

$$\frac{1}{2\pi} \int_{-\infty}^{+\infty} \hat{f}(\omega) \hat{g}(\omega) e^{i\omega t} d\omega = (f * g)(t), \quad (\text{B.3})$$

where symbol  $*$  represents the convolution product.

By using properties (B.2) and (B.3), and by enforcing the sinusoidal electric field condition, the time domain expression of the Debye relaxation model is finally derived:

$$\underline{D} = \epsilon_0 \left[ \left( \epsilon_\infty + \frac{\epsilon_s - \epsilon_\infty}{1 + \omega^2 \tau^2} \right) \underline{I} \cdot \underline{E} - \frac{\epsilon_s - \epsilon_\infty}{1 + \omega^2 \tau^2} \tau \underline{I} \cdot \dot{\underline{E}} \right]. \quad (\text{B.4})$$

Thus the reversible and irreversible parts of electric displacement and permittivity can be identified as:

$$\underline{D}^r = \epsilon_0 \left( \epsilon_\infty + \frac{\epsilon_s - \epsilon_\infty}{1 + \omega^2 \tau^2} \right) \underline{I} \cdot \underline{E} = \underline{\epsilon}^r \cdot \underline{E}, \quad (\text{B.5})$$

$$\underline{D}^i = -\epsilon_0 \frac{\epsilon_s - \epsilon_\infty}{1 + \omega^2 \tau^2} \tau \underline{I} \cdot \dot{\underline{E}} = \underline{\epsilon}^i \cdot \dot{\underline{E}}.$$

### Appendix C. Tangent matrices

This appendix reports the explicit form of tangent matrices.

$$\begin{aligned}
\mathcal{K}_{ab}^{TT} &= -\frac{\partial \mathcal{R}_a^T}{\partial a_b^T} = \int_{\Omega_e} \underline{\mathcal{B}}_a \underline{\kappa} \underline{\mathcal{B}}_b \, d\Omega_e, \\
\mathcal{K}_{ab}^{TV} &= -\frac{\partial \mathcal{R}_a^T}{\partial a_b^V} = - \int_{\Omega_e} \mathcal{N}_a \, 2 \left( \underline{\gamma} + \underline{\epsilon}^i \right) \underline{\mathcal{B}}_i \, a_i^V \underline{\mathcal{B}}_b \, d\Omega_e, \\
\mathcal{C}_{ab}^{TT} &= -\frac{\partial \mathcal{R}_a^T}{\partial \dot{a}_b^T} = \int_{\Omega_e} \mathcal{N}_a \, \rho \, c \, \mathcal{N}_b \, d\Omega_e, \\
\mathcal{K}_{ab}^{VV} &= -\frac{\partial \mathcal{R}_a^V}{\partial a_b^V} = \int_{\Omega_e} \underline{\mathcal{B}}_a \left( \underline{\gamma} + \underline{\epsilon}^i \right) \underline{\mathcal{B}}_b \, d\Omega_e, \\
\mathcal{C}_{ab}^{VV} &= -\frac{\partial \mathcal{R}_a^V}{\partial \dot{a}_b^V} = \int_{\Omega_e} \underline{\mathcal{B}}_a \underline{\epsilon}^r \underline{\mathcal{B}}_b \, d\Omega_e.
\end{aligned} \tag{C.1}$$

### Appendix D. One-dimensional analytical solution

This appendix reports the steady-state, time-independent excitation and one-dimensional analytical solution used to validate the numerical code. For this purpose, balance equation (5) in the absence of transient terms and constitutive law (21) (left) are expressed in one-dimensional form:

$$\frac{\partial j_x}{\partial x} = 0 \quad , \quad j_x = -\gamma \frac{\partial V}{\partial x}. \tag{D.1}$$

Now by considering the boundary conditions shown in Figure 1 , the voltage distribution reads:

$$V = \frac{V_2 - V_1}{L} x + V_1, \tag{D.2}$$

where  $L$  denotes the length of the one-dimensional geometry.

For the thermal field, balance equation (17) in the absence of transient terms and constitutive law (21) (middle) are expressed in one-dimensional form as:

$$\frac{\partial q_x}{\partial x} = -j_x \frac{\partial V}{\partial x} \quad , \quad q_x = -\kappa \frac{\partial T}{\partial x}. \quad (\text{D.3})$$

Finally, by enforcing the boundary conditions shown in Figure 1, the temperature distribution becomes:

$$T = -\frac{\gamma}{\kappa} \left( \frac{V_2 - V_1}{L} \right)^2 \frac{x^2}{2} + \frac{1}{L} \left[ T_2 - T_1 + \frac{\gamma}{\kappa} \left( \frac{V_2 - V_1}{L} \right)^2 \frac{L^2}{2} \right] x + T_1. \quad (\text{D.4})$$

## References

- [1] S. A. Kalogirou, “Solar thermal collectors and applications,” *Progress in Energy and Combustion Science*, vol. 30, no. 3, pp. 231 – 295, 2004.
- [2] International Energy Agency. (IEA), *Solar energy perspectives*. Paris: International Energy Agency, 2011.
- [3] Q. He, S. Wang, S. Zeng, and Z. Zheng, “Experimental investigation on photothermal properties of nanofluids for direct absorption solar thermal energy systems,” *Energy Conversion and Management*, vol. 73, pp. 150 – 157, 2013.
- [4] H. Jin, G. Lin, L. Bai, M. Amjad, E. P. B. Filho, and D. Wen, “Photothermal conversion efficiency of nanofluids: An experimental and numerical study,” *Solar Energy*, vol. 139, pp. 278 – 289, 2016.
- [5] A. Lenert and E. N. Wang, “Optimization of nanofluid volumetric receivers for solar thermal energy conversion,” *Solar Energy*, vol. 86, no. 1, pp. 253 – 265, 2012.
- [6] N. Arai, Y. Itaya, and M. Hasatani, “Development of a “volume heat-trap” type solar collector using a fine-particle semitransparent liquid suspension (FPSS) as a heat vehicle and heat storage medium Unsteady, one-dimensional heat transfer in a horizontal FPSS layer heated by thermal radiation,” *Solar Energy*, vol. 32, no. 1, pp. 49 – 56, 1984.
- [7] S. K. Verma and A. K. Tiwari, “Progress of nanofluid application in solar collectors: A review,” *Energy Conversion and Management*, vol. 100, pp. 324 – 346, 2015.
- [8] H. H. Richardson, Z. N. Hickman, A. O. Govorov, A. C. Thomas, W. Zhang, and M. E. Kordeesch, “Thermooptical properties of gold nanoparticles embedded in ice: characterization of heat generation and melting,” *Nano Letters*, vol. 6, pp. 783 – 788, 2006.
- [9] H. H. Richardson, M. T. Carlson, P. J. Tandler, P. Hernandez, and A. O. Govorov, “Experimental and Theoretical Studies of Light-to-Heat Conversion and Collective Heating Effects in Metal Nanoparticle Solutions,” *Nano Letters*, vol. 9, pp. 1139 – 1146, 2009.
- [10] M. Chen, Y. He, J. Huang, and J. Zhu, “Investigation into au nanofluids for solar photothermal conversion,” *International Journal of Heat and Mass Transfer*, vol. 108, pp. 1894 – 1900, 2017.
- [11] S. Eustis and M. A. El-Sayed, “Why gold nanoparticles are more precious than pretty gold: Noble metal surface plasmon resonance and its enhancement of the radiative and nonradiative properties of nanocrystals of different shapes,” *Chemical Society Reviews*, vol. 35, pp. 209–217, 2006.
- [12] M. Chen, Y. He, J. Zhu, and D. Wen, “Investigating the collector efficiency of silver nanofluids based direct absorption solar collectors,” *Applied Energy*, vol. 181, pp. 65 – 74, 2016.
- [13] S. Polvongsri and T. Kiatsiriroat, “Performance Analysis of Flat-Plate Solar Collector Having Silver Nanofluid as a Working Fluid,” *Heat Transfer Engineering*, vol. 35, no. 13, pp. 1183–1191, 2014.
- [14] J. Pérez-Juste, I. Pastoriza-Santos, L. M. Liz-Marzán, and P. Mulvaney, “Gold nanorods: Synthesis, characterization and applications,” *Coordination Chemistry Reviews*, vol. 249, no. 17, pp. 1870 –

- 1901, 2005. 36th International Conference on Coordination Chemistry, Merida, Mexico, July 2004.
- [15] A. Gimeno-Furio, L. Hernandez, N. Navarrete, and R. Mondragon, "Characterisation study of a thermal oil-based carbon black solar nanofluid," *Renewable Energy*, vol. 140, pp. 493 – 500, 2019.
- [16] S. Choi and J. Eastman, "Enhancing thermal conductivity of fluids with nanoparticles," *Proceedings of the ASME International Mechanical Engineering Congress and Exposition, San Francisco, CA, USA*, 1995.
- [17] T. P. Otanicar, P. Phelan, and J. S. Golden, "Optical properties of liquids for direct absorption solar thermal energy systems," *Solar Energy*, vol. 83, no. 7, pp. 969–977, 2009.
- [18] T. P. Otanicar, P. E. Phelan, R. S. Prasher, G. Rosengarten, and R. A. Taylor, "Nanofluid-based direct absorption solar collector," *Journal of Renewable and Sustainable Energy*, vol. 2, no. 3, p. 033102, 2010.
- [19] R. Taylor, S. Coulombe, T. Otanicar, P. Phelan, A. Gunawan, W. Lv, G. Rosengarten, R. Prasher, and H. Tyagi, "Small particles, big impacts: A review of the diverse applications of nanofluids," *Journal of Applied Physics*, vol. 113, no. 1, p. 011301, 2013.
- [20] R. A. Taylor, P. E. Phelan, T. P. Otanicar, R. Adrian, and R. Prasher, "Nanofluid optical property characterization: towards efficient direct absorption solar collectors," *Nanoscale Research Letters*, vol. 6, p. 225, 2011.
- [21] A. Gimeno-Furió, E. Juliá, S. Barison, F. Agresti, C. Friebe, and M. Buschmann, "Nanofluids as Direct Solar Energy Absorbers," *Journal of Nanofluids*, vol. 8, no. 1, pp. 17–29, 2019.
- [22] N. Hordy, D. Rabilloud, J.-L. Meunier, and S. Coulombe, "High temperature and long-term stability of carbon nanotube nanofluids for direct absorption solar thermal collectors," *Solar Energy*, vol. 105, pp. 82 – 90, 2014.
- [23] F. Javadi, R. Saidur, and M. Kamalisarvestani, "Investigating performance improvement of solar collectors by using nanofluids," *Renewable and Sustainable Energy Reviews*, vol. 28, pp. 232 – 245, 2013.
- [24] C. L. Beicker, M. Amjad, E. P. B. Filho], and D. Wen, "Experimental study of photothermal conversion using gold/water and mwcnt/water nanofluids," *Solar Energy Materials and Solar Cells*, vol. 188, pp. 51 – 65, 2018.
- [25] J. Lee, A. O. Govorov, and N. A. Kotov, "Nanoparticle assemblies with molecular springs: a nanoscale thermometer," *Angewandte Chemie International Edition in English*, vol. 44, no. 45, pp. 7439–7442, 2005.
- [26] C. Gota, K. Okabe, T. Funatsu, Y. Harada, and S. Uchiyama, "Hydrophilic Fluorescent Nanogel Thermometer for Intracellular Thermometry," *Journal of the American Chemical Society*, vol. 131, no. 8, pp. 2766–2767, 2009.
- [27] C. M. Tan, J. Jia, and W. Yu, "Temperature dependence of the field emission of multiwalled carbon



- nanotubes,” *Applied Physics Letters*, vol. 86, p. 263104, 2005.
- [28] M. Honda, Y. Saito, N. I. Smith, K. Fujita, and S. Kawata, “Nanoscale heating of laser irradiated single gold nanoparticles in liquid,” *Optics Express*, vol. 19, pp. 12375–12383, Jun 2011.
- [29] F. Torres and B. Jecko, “Complete FDTD analysis of microwave heating processes in frequency-dependent and temperature-dependent media,” *IEEE Transactions on Microwave Theory and Techniques*, vol. 45, pp. 108–117, 1997.
- [30] Y. Alpert and E. Jerby, “Coupled thermal-electromagnetic model for microwave heating of temperature-dependent dielectric media,” *IEEE Transactions on Plasma Science*, vol. 27, pp. 555–562, 1999.
- [31] L. Acevedo, S. Usón, and J. Uche, “Exergy transfer analysis of microwave heating systems,” *Energy*, vol. 68, pp. 349 – 363, 2014.
- [32] L. Landau and E. Lifshitz, *Electrodynamics of Continuous Media*. Oxford: Pergamon, 1984.
- [33] X. Zhao, L. Yan, and K. Huang, “Review of Numerical Simulation of Microwave Heating Process,” in *Advances in Induction and Microwave Heating of Mineral and Organic Materials* (S. Grundas, ed.), ch. 2, London: IntechOpen, 2011.
- [34] K. Huang and Y. Liao, “Transient Power Loss Density of Electromagnetic Pulse in Debye Media,” *IEEE Transactions on Microwave Theory and Techniques*, vol. 63, pp. 135–140, 2015.
- [35] P. Castiglione and P. Shouse, “The effect of ohmic cable losses on time-domain reflectometry measurements of electrical conductivity,” *Soil Science Society of America Journal*, vol. 67, pp. 414–424, 2003.
- [36] S. R. de Groot and P. Mazur, *Non-Equilibrium Thermodynamics*. New York: Dover Publications, Inc., 1984.
- [37] G. Lebon, D. Jou, and J. Casas-Vázquez, *Understanding Non-equilibrium Thermodynamics*. New York: Springer-Verlag Berlin Heidelberg, 2008.
- [38] F. Bresme, A. Lervik, D. Bedeaux, and S. Kjelstrup, “Water Polarization under Thermal Gradients,” *Physical Review Letters*, vol. 101, p. 020602, 2008.
- [39] L. Restuccia and G. A. Kluitenberg, “On the heat dissipation function for dielectric relaxation phenomena in anisotropic media,” *International Journal of Engineering Science*, vol. 30, no. 3, pp. 305 – 315, 1992.
- [40] F. Farsaci and P. Rogolino, “An alternative dielectric model for low and high frequencies: A non-equilibrium thermodynamic approach,” *Journal of Non-Equilibrium Thermodynamics*, vol. 37, pp. 27–41, 2012.
- [41] P. Debye, *Polar Molecules*. New York: The Chemical Catalog Company, Inc., 1929.
- [42] H. B. Callen, *Thermodynamics and an Introduction to Thermostatistics*. New York: John Wiley and Sons, Inc., 1985.

- [43] O. Zienkiewicz and R. Taylor, *The Finite Element Method 7th Edition*. Oxford: Butterworth-Heinemann, 2013.
- [44] R. Taylor, *FEAP A Finite Element Analysis Program: User Manual*. University of California, Berkeley, 2013. <http://www.ce.berkeley.edu/feap>.
- [45] S. Bruzzone and M. Malvaldi, “Local Field Effects on Laser-Induced Heating of Metal Nanoparticles,” *The Journal of Physical Chemistry C*, vol. 113, no. 36, pp. 15805–15810, 2009.
- [46] J. Pérez-Aparicio, R. Palma, and R. Taylor, “Multiphysics and thermodynamic formulations for equilibrium and non-equilibrium interactions: non-linear finite elements applied to multi-coupled active materials,” *Archives of Computational Methods in Engineering*, vol. 23, no. 3, pp. 535–583, 2016.
- [47] R. Tinder, *Tensor Properties of Solids: Phenomenological Development of the Tensor Properties of Crystals*. Morgan and Claypool Publishers, 2008.
- [48] R. Taylor, *FEAP A Finite Element Analysis Program: Programmer Manual*. University of California, Berkeley, 2014. <http://www.ce.berkeley.edu/feap>.
- [49] R. H. Perry, D. W. Green, and J. O. Maloney, *Perry’s Chemical Engineers’ Handbook*. New York: McGraw-Hill, 2008.
- [50] *ASM Handbook Volume 2: Properties and Selection: Nonferrous Alloys and Special-Purpose Materials*. Materials Park: ASM International, 1990.
- [51] S. Kasap, C. Koughia, and H. E. Ruda, “Electrical conduction in metals and semiconductors,” in *Springer Handbook of Electronic and Photonic Materials* (S. Kasap and P. Capper, eds.), ch. 2, New York: Springer International Publishing, 2017.
- [52] D. I. Yakubovsky, A. V. Arsenin, Y. V. Stebunov, D. Y. Fedyanin, and V. S. Volkov, “Optical constants and structural properties of thin gold films,” *Optics Express*, vol. 25, no. 21, pp. 25574–25587, 2017.
- [53] M. Polyanskiy, “Refractiveindex.info website.” <https://refractiveindex.info/>. Last Accessed: 18-02-2020.
- [54] K. M. Chew, R. Sudirman, N. Seman, and C. Y. Yong, “Relaxation frequency and relaxation time estimation for phantom modeling by proposed fitting linear models,” in *2012 IEEE-EMBS Conference on Biomedical Engineering and Sciences*, pp. 911–915, 2012.
- [55] R. Richert, A. Agapov, and A. P. Sokolov, “Appearance of a Debye process at the conductivity relaxation frequency of a viscous liquid,” *The Journal of Chemical Physics*, vol. 134, no. 10, p. 104508, 2011.
- [56] Lenntech, “Water conductivity.” <https://www.lenntech.com/applications/ultrapure/conductivity/water-conductivity.htm>. Last Accessed: 02-05-2019.
- [57] G. M. Hale and M. R. Querry, “Optical Constants of Water in the 200-nm to 200- $\mu$ m Wavelength

- Region,” *Applied Optics*, vol. 12, no. 3, pp. 555–563, 1973.
- [58] J. P. A. Bastos and N. Sadowski, *Electromagnetic Modeling by Finite Element Methods*. Washington, D.C.: CRC Press, 2003.
- [59] A. Ciesielski, L. Skowronski, M. Trzcinski, and T. Szoplik, “Controlling the optical parameters of self-assembled silver films with wetting layers and annealing,” *Applied Surface Science*, vol. 421, pp. 349 – 356, 2017. 7th International Conference on Spectroscopic Ellipsometry.
- [60] H. O. Pierson, *Handbook of Carbon, Graphite, Diamonds and Fullerenes*. New Jersey: Noyes Publications, 1994.
- [61] M. R. Query, *Optical Constants*. Kansas City: Defense Technical Information Center. Department of Defense, USA, 1985.
- [62] Y. J. Zhang, “Investigation of Gold and Silver Nanoparticles on Absorption Heating and Scattering Imaging,” *Plasmonics*, vol. 6, no. 2, pp. 393–397, 2011.
- [63] J. Theerthagiri, R. Sudha, K. Premnath, P. Arunachalam, J. Madhavan, and A. M. Al-Mayouf, “Growth of iron diselenide nanorods on graphene oxide nanosheets as advanced electrocatalyst for hydrogen evolution reaction,” *International Journal of Hydrogen Energy*, vol. 42, no. 18, pp. 13020 – 13030, 2017.
- [64] M. Mehrali, M. K. Ghatkesar, and R. Pecnik, “Full-spectrum volumetric solar thermal conversion via graphene/silver hybrid plasmonic nanofluids,” *Applied Energy*, vol. 224, pp. 103 – 115, 2018.
- [65] T. B. Gorji and A. Ranjbar, “A numerical and experimental investigation on the performance of a low-flux direct absorption solar collector (DASC) using graphite, magnetite and silver nanofluids,” *Solar Energy*, vol. 135, pp. 493 – 505, 2016.
- [66] S. S. Murshed and P. Estellé, “Rheological characteristics of nanofluids for advance heat transfer,” in *Advances in New Heat Transfer Fluids: From Numerical to Experimental Techniques* (A. A. Minea, ed.), ch. 9, Boca Raton: CRC Press, 2017.
- [67] F. Yu, Y. Chen, X. Liang, J. Xu, C. Lee, Q. Liang, P. Tao, and T. Deng, “Dispersion stability of thermal nanofluids,” *Progress in Natural Science: Materials International*, vol. 27, no. 5, pp. 531 – 542, 2017.
- [68] S. U. Ilyas, R. Pendyala, M. Narahari, and L. Susin, “Stability, rheology and thermal analysis of functionalized alumina- thermal oil-based nanofluids for advanced cooling systems,” *Energy Conversion and Management*, vol. 142, pp. 215 – 229, 2017.
- [69] N. Singh and V. Khullar, “Efficient volumetric absorption solar thermal platforms employing thermally stable - solar selective nanofluids engineered from used engine oil,” *Scientific Reports*, vol. 9, no. 1, p. 10541, 2019.
- [70] M. Onimisi and T. Ikyumbur, “Comparative analysis of dielectric constant and loss factor of pure butan-1-ol and ethanol,” *American Journal of Condensed Matter Physics*, vol. 2015, pp. 69–75, 10

2015.